Biosensors and Bioelectronics 210 (2022) 114235

Contents lists available at ScienceDirect

Biosensors and Bioelectronics

journal homepage: www.elsevier.com/locate/bios

Ultra-sensitive dielectrophoretic surface charge multiplex detection inside a micro-dielectrophoretic device

Kang In Yeo [a,1], Insu Park [b,1], Sang Hyun Lee [a], Sei Young Lee [a], Woo-Jin Chang [c], Rashid Bashir [b,d,e,f], Seungyeop Choi [a,**], Sang Woo Lee [a,*]

[a] Department of Biomedical Engineering, Yonsei University, Wonju, 26493, Republic of Korea
[b] Holonyak Micro and Nanotechnology Laboratory, University of Illinois at Urbana—Champaign, Urbana, IL, 61801, USA
[c] Mechanical Engineering Department, University of Wisconsin-Milwaukee, Milwaukee, WI, 53211, USA
[d] Department of Mechanical Science and Engineering, University of Illinois at Urbana—Champaign, Urbana, IL, 61801, USA
[e] Department of Bioengineering, University of Illinois at Urbana—Champaign, Urbana, IL, 61801, USA
[f] Materials Research Laboratory, University of Illinois at Urbana—Champaign, Urbana, IL, 61801, USA

ARTICLE INFO

Keywords:
Multiplex detection
Label free
Dielectrophoresis
Surface charge
Ultra-sensitive
Micro-dielectrophoretic device

ABSTRACT

Label-free dielectrophoretic force-based surface charge detection has shown great potential for highly sensitive and selective sensing of metal ions and small biomolecules. However, this method suffers from a complex calibration process and measurement signal interference in simultaneous multi-analyte detection, thus creating difficulties in multiplex detection. We have developed a method to overcome these issues based on the optical discrimination of the dielectrophoretic behaviors of multiple microparticle probes considering the surface charge difference before and after self-assembling conjugation. In this report, we demonstrate and characterize this dielectrophoretic force-based surface charge detection method with particle probes functionalized by various biomolecules. This technique achieved an attomolar limit of detection (LOD) for Hg^{2+} in distilled water and a femtomolar LOD in drinking water using DNA aptamer-functionalized particle probes. More importantly, using two different DNA aptamer-functionalized particle probes for Hg^{2+} and Ag^{+}, label-free dielectrophoretic multiplex detection of these species in drinking water with a femtomolar and a nanomolar LOD was achieved for the first time.

1. Introduction

Over the past few decades, numerous biosensors have been developed for the detection of diverse analytes, including antibodies, DNA, cells, and other small molecules (Chalklen et al., 2020; Goode et al., 2015). Based on an investigation of the physicochemical properties of biomolecules, researchers have exploited various detection methodologies (e.g., optical, electrochemical, and mechanical-based methodologies) to identify minute analyte quantities (Chalklen et al., 2020; Khan and Song, 2020). Among these techniques, electrochemical biosensors, which are based on electron detection, have attracted increasing attention due to their high sensitivity, low cost, and ease of miniaturization enabled by a combination of advanced microfabrication techniques and high-resolution decoding techniques (Grieshaber et al., 2008; Luo and Davis, 2013; Ronkainen et al., 2010). Moreover, integration with surface science allows for a surface charge/potential sensor with the advantages of ultra-high sensitivity and label-free detection. Excellent examples of such approaches include Kelvin probe force microscopy (KPFM), field-effect transistors (FET), and nanopore sensing (Melitz et al., 2011; Shi et al., 2017; Vu and Chen, 2019). These examples demonstrate femtomole-level (and even attomole-level) sensitivity without any complicated pre-labeling procedures, while maintaining the advantages of general electrochemical biosensors (Chen et al., 2020). Therefore, surface charge/potential sensors show the promise for ultra-sensitive detection.

Another important issue in the development of biosensors is multiple-analyte detection. Multiplex detection improves efficiency and ensures high throughput. Moreover, the detection of more than one

* Corresponding author.
** Corresponding author.
E-mail addresses: seungyeop.choi@yonsei.ac.kr (S. Choi), yusuklee@yonsei.ac.kr (S.W. Lee).
[1] These authors contributed equally to this work.

https://doi.org/10.1016/j.bios.2022.114235
Received 6 December 2021; Received in revised form 22 March 2022; Accepted 28 March 2022
Available online 14 April 2022

analyte is critically important both in the detection of immunity for early disease diagnostics and in the detection of microbes or metal ions for food inspection and environmental assessment (Li et al., 2018b; Liu et al., 2018; Luo and Davis, 2013; Su et al., 2011; Yin et al., 2020). In multiplex detection, optical detection methods are commonly used due to a number of advantages. Probes that simultaneously detect different optical signals are simple and robust (Chen and Wang, 2020; Liao et al., 2019). For multiple analyte detection, high-speed encoding and decoding through the optical signals can be easily achieved (Fan et al., 2019). In these respects, optical detection is superior to surface charge/potential detection since surface charge/potential methods generally require more complicated and less robust probes and a complex calibration step for accurate measurement (Mayne et al., 2018; Shahim et al., 2019; Vacic et al., 2011). It is also difficult to avoid the interference between probes during measurement (Pakchin et al., 2017; Yáñez-Sedeño et al., 2017). On the other hand, in optical multiplex detection, extra labeling procedures are necessary to achieve high sensitivity or high selectivity (Díaz-González et al., 2020; Shan et al., 2018). Hence, according to our survey of the literature, the integration of the advantages of both methods can overcome such issues and would play a pivotal role in advancing early disease diagnostics, food inspection, and environmental assessment.

Dielectrophoresis is a well-known tool to efficiently control the movement of micro and nano-sized particles in a non-uniform electric field based on their electrical properties (Abd Rahman et al., 2017). The efficient controllability of this method has been widely used for many bioparticles and biologically functionalized particles for enrichment and detection through processes such as trapping, alignment, and separation (Chen and Yuan, 2019; Hölzel and Pethig, 2020; Viefhues and Eichhorn, 2017). Furthermore, such well-controlled movements can be easily observed and detected using an optical detection method (Hoettges et al., 2008; Yafouz et al., 2014). Recent developments in dielectrophoresis techniques have enabled the determination of surface charge differences through the observation of the behavior of numerous micro-objects, which function as probes, that can be detected inside a micro-dielectrophoretic device using a dielectrophoretic (DEP) tweezers-based force spectroscopy (Choi et al. 2016, 2018; Park et al. 2012, 2015b, 2016, 2020; Son et al., 2016). This technique is able to compare the surface charges of individual bio-particles through the observation of the particles' DEP behaviors, since the behaviors of individual bio-particles with different surface charges are distinguishable under a DEP force. Moreover, it is not necessary to perform a complex calibration to detect the surface charge differences of the particles. While the observation detects charge differences, it easily avoids the interference generated from each of the other objects. More importantly, within a certain electrical frequency region, the DEP behavior of each particle responding to surface charge difference is extremely sensitive.

In this study, we develop an ultra-sensitive method to simultaneously detect the surface charge difference of numerous micro-particle probes in the same environment using observations of the probes' vertical movements controlled by DEP force inside a micro-dielectrophoretic device. In our method, optical detection enables the detection of the surface charge difference of each particle. As a proof of concept of the developed method, the surface charge differences of various biomolecules, such as carboxyl-functionalized on carbon-hydrogen molecules, streptavidin, DNA, and DNA-heavy metal ion complexes were detected and characterized. We also evaluated the sensitivity and selectivity of the developed method by examining numerous DNA-Hg^{2+} complex particle probes without additional labeling. Furthermore, we demonstrated, for the first time, a label-free DEP multiplex metal ion assay by the surface charge difference between DNA-Hg^{2+} complex and DNA-Ag^{+} complex particle probes, which exhibits excellent selectivity and sensitivity for each heavy metal ions.

2. Materials and methods

2.1. Materials and reagents

All deoxyoligonucleotides were synthesized and HPLC-purified by Cosmogenetech (Seoul, Republic of Korea). The sequences of oligonucleotide are listed in Table 1. Plain polystyrene particles (10 μm-radius) and carboxyl group-functionalized polystyrene particles (10, 15 μm-radius) were purchased from Micromod (Rostock, Germany). Streptavidin-immobilized particles (10 μm) were purchased from Spherotech (Lake Forest, Illinois, USA). 1-ethyl-3-(3-dimethylaminopropyl) carbodiimide hydrochloride (EDC), N-hydroxysuccinimide (NHS), 2-(n-morpholino) ethanesulfonic acid hydrate (MES hydrate), Biotin, $AgNO_3$, $CaCl_2$, $CuCl_2$, $FeCl_3$, $HgCl_2$, $MgCl_2$, $MnCl_2$, $NiCl_2$ and Tris-EDTA buffer solution were purchased from Sigma-Aldrich (St. Louis, Missouri, USA). Phosphate-buffered saline (PBS) was purchased from Gibco (Gaithersburg, MD, USA). Deionized (DI) water was obtained from a purification system from Sartorius AG (Gottingen, Germany). Drinking water was purchased from Nestlé waters (Nestlé Pure Life, Paris, France).

2.2. Formation of streptavidin-biotin complex

10 μM biotin stock solution was prepared by dissolving pure 99% biotin molecule in PBS buffer. Streptavidin-particles were added to the biotin stock solution (1.86×10^5 particles mL^{-1}) and incubated for 1 h. Subsequently, the solutions were rinsed with 2 μM PBS buffer in which the conductivity was measured to be 35 μS/cm.

2.3. Functionalization of oligonucleotides on microparticle probes

To demonstrate the concept of the proposed methodology, which can be used to identify variation of negative surface charges on microparticles, the surface of microparticles were functionalized with various oligonucleotides (Table 1). Specifically, 3 mg/mL carboxyl group-functionalized polystyrene particles were prepared in 1 M MES buffer. The carboxyl groups on the particles were activated with both 3 mg EDC and 10 mg NHS for 30 min. After being rinsed with 1M MES buffer using centrifugation for eliminating free EDC and NHS molecules, 5 μM of amine-modified oligonucleotide was added and stirred in the reaction mixture overnight. The resulting coated particles were purified four times by centrifugation and resuspension in deionized water.

2.4. Formation of DNA hybridization complex

DNA-DNA hybridization reaction was conducted between the poly-6 thymine single strand DNA (6T) coated on 10 μm particle surfaces and the poly-6 adenine single strand DNA (6A). To generate a hybridization reaction, 1 μM 6A DNA solutions were prepared in Tris-EDTA buffer and

Table 1
Sequences of the DNA oligonucleotides. A, T, C, and G represent the nucleotide bases of adenine, thymine, cytosine, and guanine, respectively, in the DNA sequences. Bold characters represent the ligand-binding site that are complementary in structure to a specific metal ion (32 nt aptamer for Ag^{+} (Ono et al., 2008) and 28 nt aptamer for Hg^{2+} (Chen et al., 2012)), respectively.

Name	Modification Name	DNA Sequence (5'→3')	Usage
6T	5′–NH_2–$(CH_2)_{12}$	TTT TTT	probe for 6A
6A	W/O modification	AAA AAA	target for 6T
28 nt	5′–NH_2–$(CH_2)_{12}$	**TTT** C**TT** **TCT** **T**CC CCC CGG **TT**G **TTT** G**TT** A	probe for Hg^{2+}
32 nt	5′–NH_2–$(CH_2)_{12}$	**CTC** **TCT** TCT C**TT** **CAT** TTT **TCA** **ACA** **CAA** **CAC** **AC**	probe for Ag^{+}

10 mM NaCl solution. The 6T DNA immobilized particle solutions were added to the 6A DNA solution (1.86×10^5 particles mL^{-1}), and incubated for 1 h at 40 °C. Subsequently, the solution was cooled to room temperature for 1 h. Particle-DNA solutions were then washed with DI water. Then, solutions were rinsed with 35 μS/cm conductivity water made with 2 μM PBS to yield 6A DNA hybridized 6T DNA (6T+6A)-coated 10 μm particles.

2.5. Formation of DNA-metal ion complex

All metal solutions including Ag^+, Ca^{2+}, Cu^{2+}, Fe^{3+}, Hg^{2+}, Mg^{2+}, Mn^{2+}, and Ni^{2+} ions were prepared in deionized water or drinking water. DNA-immobilized micro-particles were added to the metal ion solutions (1.86×10^5 particles mL^{-1}) and incubated for 1 h. Subsequently, the solutions were rinsed with 2 μM PBS buffer in which the conductivity was measured to be 35 μS/cm.

2.6. Zeta potential measurement

The Zeta potential measurements (Zetasizer Nano ZS90 (Malvern Instruments, Malvern, UK)) were performed to characterize the charges of the microparticles, which were plain vs. carboxylated particle, streptavidin vs. streptavidin-biotin functionalized particle, 6T vs. 6T+6A coated particle, and 28 nt vs. 28 nt-Hg^{2+} coated particle. Tested particles were immersed in the test buffer mentioned above (1.86×10^5 particles mL^{-1}) separately. The individual particle solutions were sonicated in an ultrasonic bath for 3 min to disperse the particles in the sample. The Samples were injected in a Zetasizer cell (Malvern, DTS1070) for the zeta potential analysis. Each measurement was conducted 10 times (Fig. 3C).

2.7. DEP experimental procedures

On the 8 mm wide, 20 mm high DEP chip, a PDMS circular donut-shaped reservoir was attached to contain the micro-particle solutions. Liquid containing 10-μm-radius particles, 15-μm-radius particles, or 10-μm and 15-μm-radius particles was injected into the inner circular area and covered with cover-glass to prevent evaporation of the solutions. Subsequently, we applied the DEP signal to the DEP chip and observed the microparticles using the customized probe station (the set-up image is shown in Fig. S11). An initial input voltage of 0.6 $V_{p\text{-}p}$ and frequency of 350 kHz was applied by a function generator (NI PCI-5421, National Instrument, Austin, TX, USA). Top-view images of the DEP system were captured at a rate of 1 frame per second by a CCD camera connected to a bright-field microscope. Next, the frequency was decreased by steps from 350 to 75 kHz, at a rate of 1 kHz/s, with 5 s pause at each new frequency (e.g., step from 350 to 349 kHz in 1 s, wait for 4 s at 349 kHz, then step down to 348 kHz).

3. Results and discussion

3.1. Characterization of the dielectrophoretic surface charge detection method

3.1.1. Operating background of the DEP surface charge detection method

Fig. 1A illustrates the system that is developed to detect surface charge differences for various types of biomolecules through the observation of the vertical movements of microparticle probes. When

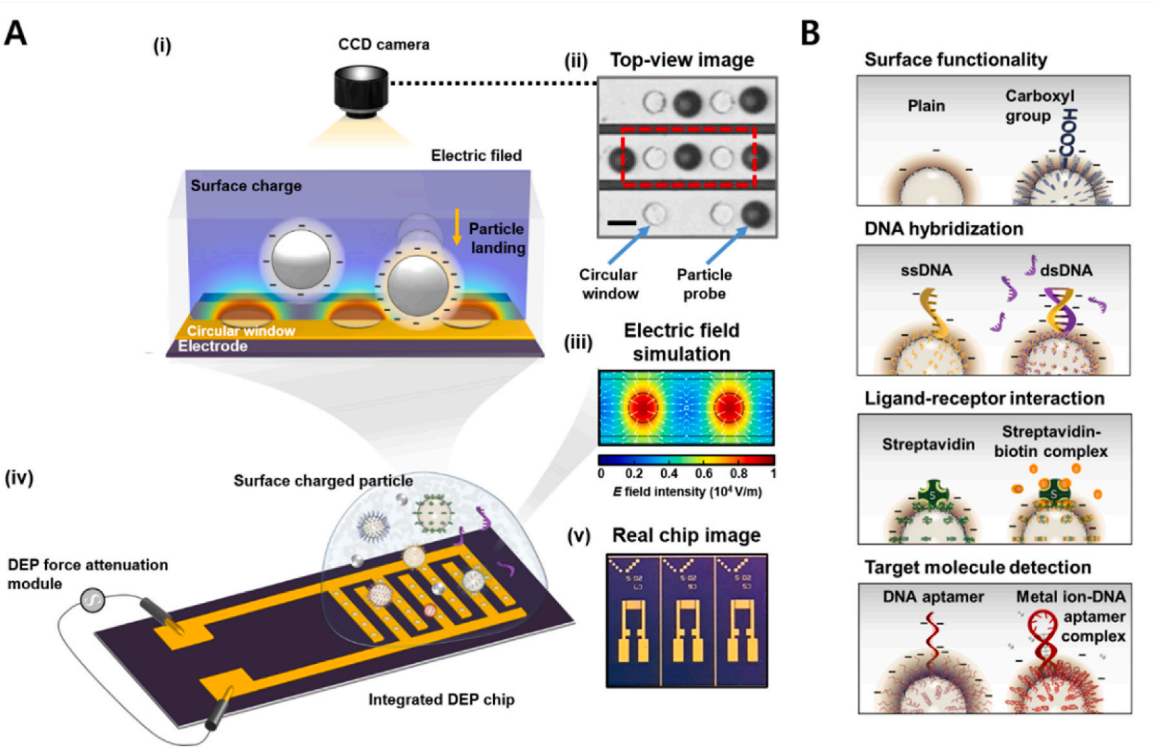

Fig. 1. Designs for a DEP-based surface charge detection system. (**A**) Schematic of a DEP-based surface charge detection system using microparticle probes on an interdigitated DEP chip. (A-i) Non-uniform electric fields on the DEP chip induce difference of vertical motions of particle probes depending on their surface charge. (A-ii) In this system, microparticle probes' vertical motion was observed using top-view of microscope image (AC 0.6 $V_{p\text{-}p}$, 350 kHz). Scale bar is 10 μm. (A-iii) The simulated results of electric field distribution and DEP force direction at 5 μm height inside the red box that includes the circular window pattern of the etched passivated layer on the electrode, which can make the particle probes to be located individually between two circular windows by a negative DEP force (more detailed description is in Fig. S10). (A-iv) The schematic of DEP chip image shows the various types of particle probes introduced on the DEP chip while input AC voltage are applied. (A-v) The real photograph of DEP chips. (**B**) Particle probes functionalized by biomolecules (a simple chemical group, protein, ssDNA, dsDNA, and DNA aptamer and a metal ion-DNA aptamer complex) for detection of their surface charge differences.

the probes with different surface charges are in the non-uniform electrical field in the chip, the vertical position of the probes is determined by the equilibrium position between the sedimentary force and vertical DEP force, as shown in Fig. 1A. To demonstrate the ability of this system to detect surface charge in diverse systems, four different methods of changing surface charge with functionalized particle probes were considered, as shown in Fig. 1B: surface functionalization, ligand-receptor interaction, DNA hybridization and target molecule detection. As an example of detecting charge due to surface functionality, plain and carboxylated particles were interrogated. Streptavidin- and streptavidin-biotin-coated particles were used to investigate surface charge differences due to ligand-receptor interaction. Detection of DNA hybridization was explored through the use of ssDNA- and dsDNA-coated particles. A DNA aptamer functionalized particle with and without metal ion chelation was used to demonstrate target molecule detection. Specifically, we prepared the mercury ion (II) and silver ion (I)-specific binding DNA aptamer sequence that validated in previous reports, respectively (Chen et al., 2012; Ono et al., 2008). The surface charge discrimination was conducted via the following procedure. When a solution with the surface functionalized particle probes is introduced in the interdigitated DEP chip shown in Fig. 1A-i and 1A-iv, the probes are randomly distributed in the absence of the non-uniform electric field. Under an applied electric field with a particular frequency, the probes align between two circular windows, as shown in Fig. 1A-ii, which corresponds to a negative DEP force acting on the probes (a detailed probes' behavior under a DEP force is described in Supplementary Note 1). The particle probes align at a height from a DEP chip substrate where the sedimentary force and the vertical DEP force acting on the probes are balanced when an electrical signal is applied. An example of balanced particle probes is shown in Fig. 1A-ii. The state that has the balanced particle probes (e.g., particles shown in Fig. 1A-ii, which are further used to observe their vertical movement as a function of decreasing DEP force, is defined as the initial state for beginning the DEP surface charge detection method.

3.1.2. *Measurement principle of the DEP surface charge detection method*

As the input frequency decreases, the vertical location that the DEP force balances with sedimentary force is lowered due to redistribution of the vertical electric field gradient. As a result, the particle probes move vertically down from the initial state to the next levitation state, which is newly determined by the decreasing input frequency. Fig. 2A presents images of the plain particle probes at four representative input frequencies: 350, 250, 150, and 75 kHz. From the initial state of input voltage 0.6 $V_{p\text{-}p}$ and input frequency 350 kHz, the input frequency is lowered to 75 kHz with fixed input voltage. The input frequency is lowered at 1 kHz/s with a 4 s stabilization period at each levitation state. As shown in Fig. 2A, the brightness intensity of the particle images ($I_{particle}$) changes as the input frequency is lowered (the individual particle imaging is shown in Supplementary Movie S1). The variation of the vertical particle location can be quantitatively mapped to the variation of the brightness intensity of the particle images as a function of frequency, and this method was previously introduced by our group (Choi et al., 2016; Park et al. 2012, 2016; Son et al., 2016). Fig. 2B shows the normalized brightness intensity variation of the particle probes when the input frequency was decreased. The normalization of brightness intensity was conducted by baseline correction using the last 50 frames of observed particle images. The normalized brightness intensity within the particle image ($\Delta I_{particle}$) increases from its minimum value at the initial state (e.g., −61 at 350 kHz, Fig. 2B inset) to its maximum value (e.g., 75 at 186 kHz, Fig. 2B inset). As shown in Fig. 2B, once $\Delta I_{particle}$ reaches its maximum value, it can be assumed that $\Delta I_{particle}$ decreases quasi-linearly with a constant slope until it reaches a certain critical value (e.g., 0–4 around 132 kHz in Fig. 2B) and then follows a linear relationship with a different slope. The first steep slope accounts for the dynamic variation of the $\Delta I_{particle}$ value as the particle moves down vertically before interacting with the surface, which is designated as the dynamic state. The second slope represents the region in which the particle is close to the surface so that only a small vibrating motion in the vertical direction can be observed, which is designated as the landing state. Based on these observations of the brightness intensity variation, the transition frequency ($f_{transition}$), at which the transition from the dynamic state to the landing state occurs, can be defined. To determine $f_{transition}$ experimentally, a two-line regression linear fit is employed, and the intersecting point of two lines is defined as the transition frequency (the detailed analysis process is described in Supplementary Note 2.

Supplementary data related to this article can be found at https://doi.org/10.1016/j.bios.2022.114235.

3.1.3. *Transition frequency of the particle probes decorated by various biomolecules*

Using the developed surface charge detection method, $f_{transition}$ is determined for four representative pairs of the functionalized particle

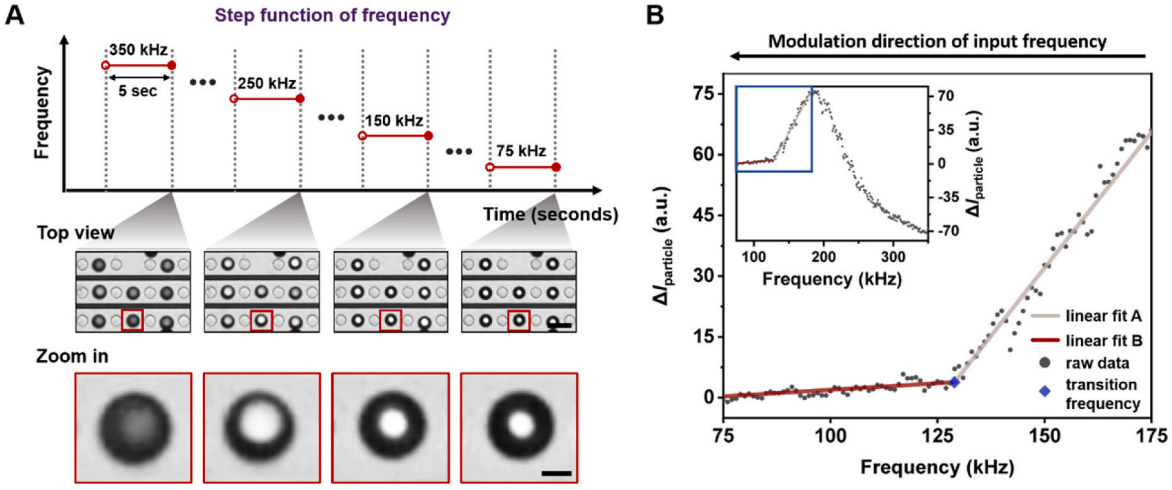

Fig. 2. Characterization of transition frequency of microprobes in DEP Surface charge detection method. (**A**) Images of vertical motion at four different frequency steps (350, 250, 150, 75 kHz) with 0.6 $V_{p\text{-}p}$. The image at 350 kHz is the initial state of a plain polystyrene particle probe with 10 μm radius just before vertical motion occurs. The remaining images are snap shots of the particle held at a certain height for 5 s after moving down vertically from the initial state (scale bars 20 and 5 μm in top-view and zoom in, respectively). (**B**) $\Delta I_{particle}$ observed from 10 μm plain particle probe images as a function of frequency, gray and red lines represent two linear regression lines to analyze the transition frequency ($f_{transition}$).

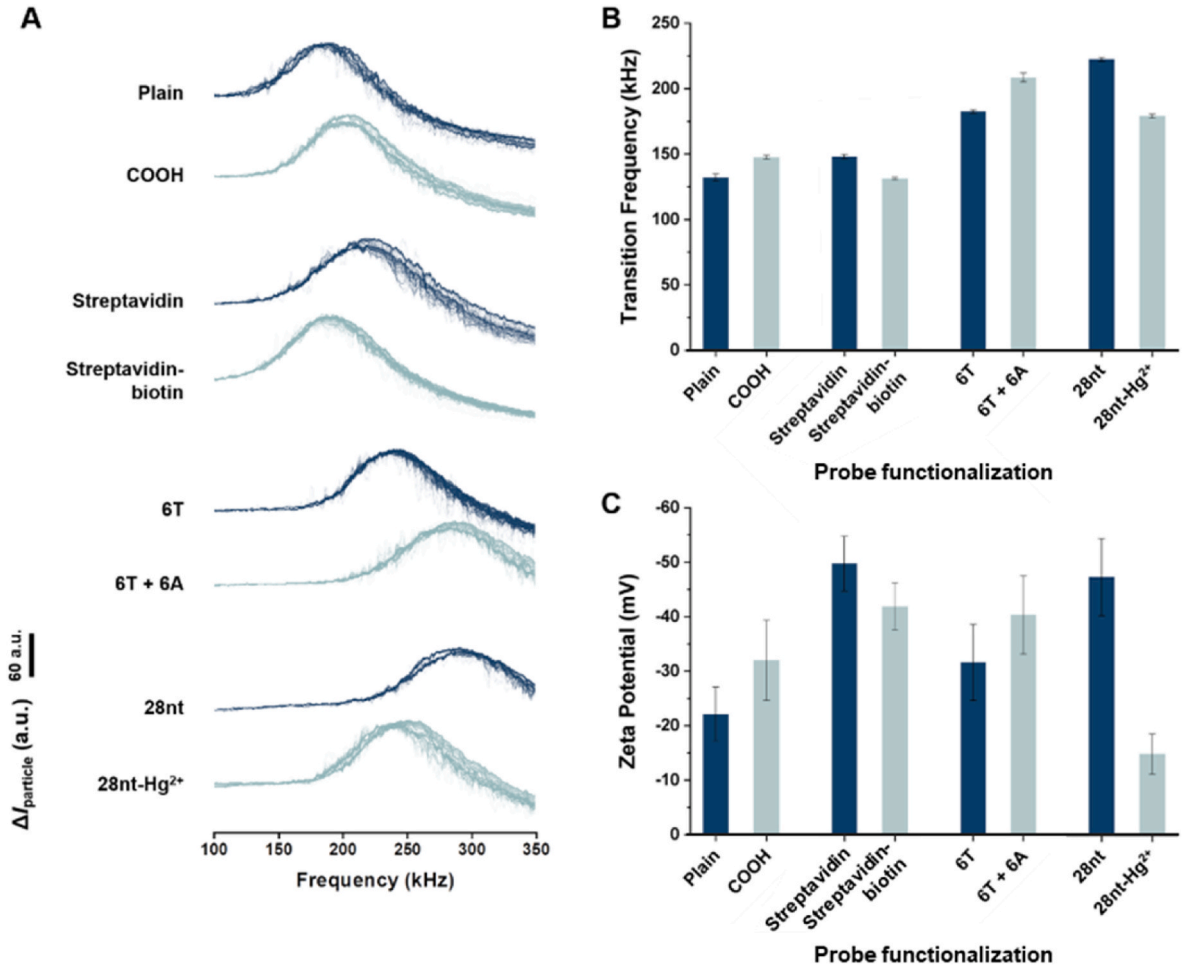

Fig. 3. Detection of the surface charge difference in various molecules. (**A**) Measured $\Delta I_{particle}$ data corresponding to the vertical movement of the plain vs. carboxylated, streptavidin vs. streptavidin-biotin complex, 6T vs. 6T+6A, 28 nt aptamer vs. Hg^{2+}-28 nt aptamer particle probes depending on the overall measurement frequency range domain. (**B**) Transition frequencies and (**C**) zeta potentials of the corresponding particle probes. The more detailed statistical analysis result between the different surface functionality in Fig. 3B is provided in Supplementary Table S1.

probes, that is, plain vs. carboxylated particle probes, streptavidin vs. streptavidin-biotin functionalized particle probes, 6T (5′-TTTTTT-3′) vs. 6T+6A (5′-AAAAAA-3′) coated particle probes, and 28 nt aptamer (5′-TTTCTTTCTTCCCCCCGGTTGTTTGTTA-3′) vs. Hg^{2+}-28 nt aptamer coated particle probes, which correspond to the examples of the surface charge variation due to surface functionality, ligand-receptor interaction, DNA hybridization, DNA aptamer target binding, respectively, where the 28 nt aptamer undergoes a conformation change of hairpin structure by T-Hg(II)-T formation when it is converted to Hg^{2+}-28 nt aptamer (Chen et al., 2012; Ono and Togashi, 2004; Torigoe et al., 2012). Since particle probes with different surface charges experience different DEP forces for a given applied frequency (Nakano et al., 2019; Park et al., 2014a) (Supplementary Note 1), the vertical movements of each particle should be different. Fig. 3A clearly shows that the developed surface charge detection method discriminates the particle probes containing different surface functionalization. Moreover, $f_{transition}$ of the functionalized particle probes is characterized by the two-line regression linear fit method, as shown in Fig. 3B. Comparing the results to the zeta potential of each functionalized particle probes shown in Fig. 3C, the probe with the greater negative zeta potential of each probe pair yields the higher $f_{transition}$ of the pair, which indicates that more negatively charged particles approaches zero force (i.e., enter the landing state) at a higher $f_{transition}$, which is in good agreement with DEP theory (Choi et al., 2018; Park et al. 2015b, 2020) (Supplementary Note 1). Furthermore, our results are also good agreement with the previous reports for surface potential/charge sensing. For example, it was reported that the positive amine group in biotin molecules was contributed to the positive surface charge formation after the generation of streptavidin-biotin complex (Chen et al., 2017; Kim et al., 2006). On the result of DNA hybridization, it is amenable that the surface charge of double strand DNA are more negative than that of single strand DNA, due to the increase of negatively charged phosphate backbone of DNA (Lee et al., 2018; Sinensky and Belcher, 2007). After 28 nt aptamer forms Hg^{2+}-28 nt aptamer, Hg^{2+} metal ion contributes to the formation of positive surface charge (Park et al. 2014b, 2015a). It should be noted that the relationship of zeta potential and $f_{transition}$, which are measured by using electrophoretic (EP) mobility generated by DC signal and dielectrophoretic (DEP) mobility generated by AC signal respectively, shows a discrepancy in the comparison between different molecular structures. As shown in Fig. 3B and C, even though the zeta potential of the streptavidin-functionalized probe is greater than that of the 6T-functionalized probe, $f_{transition}$ between streptavidin-functionalized probe and the 6T-functionalized probe is vice versa. The reason why the discrepancy occurs might come from the polarization difference by DC and AC electric field (Chiu and Ducker, 2014). For example, two particles with identical zeta-potential show a different mobility among them (Arnold et al., 1987). Another reason for the discrepancy might be from the complexity of streptavidin molecular structure. When the molecular complexity can be composed with a nonlinear charge distribution from the particle surface, zeta potential is not properly contributed to

represent the actual molecular charge (Vorwerg et al., 1999; Mayne et al., 2018). Further investigation should be needed to understand the discrepancy more clearly. However, it can be safely said that our developed detection method can work properly since the method uses not an exact value of surface charge but a surface charge difference of each different molecule for the detection. Overall, Fig. 3 clearly shows that the developed surface charge detection method is capable of distinguishing various biomolecules for the development of the multiplex detection using different particles as multiplex probes.

3.2. Evaluation of the dielectrophoretic surface charge detection method

3.2.1. Sensitivity evaluation of the DEP surface charge detection method

To compare the detection capability of the developed method to previously reported surface charge detection methods, which have femtomolar (fM) limit of detection (LOD) for various target molecules (Chen et al., 2020; Khan and Song, 2020; Pourali et al., 2021), 28 nt aptamer-coated particle probes were selected as prototype probes to detect a wide range of Hg^{2+} concentrations (Chen et al., 2012). Sequential images of the functionalized particle probes are captured as the input frequency decreases for various Hg^{2+} concentrations from 10 aM to 10 μM, and the normalized brightness intensity of the sequential images are plotted in Fig. 4A for each Hg^{2+} concentration. Based on the normalized brightness intensity plot, absolute difference of transition frequency between with/without metal ion, $|\Delta(f_{transition-ion} - f_{transition-control})|$ is determined for each Hg^{2+} concentration, as shown in Fig. 4B. Particularly, the current DEP charge detection method measures numerous probes (~2×10^2 particles/mm^2) simultaneously in the exact same environment. Fig. 4B shows the linear relationship between $f_{transition}$ and Hg^{2+} concentration. Moreover, the

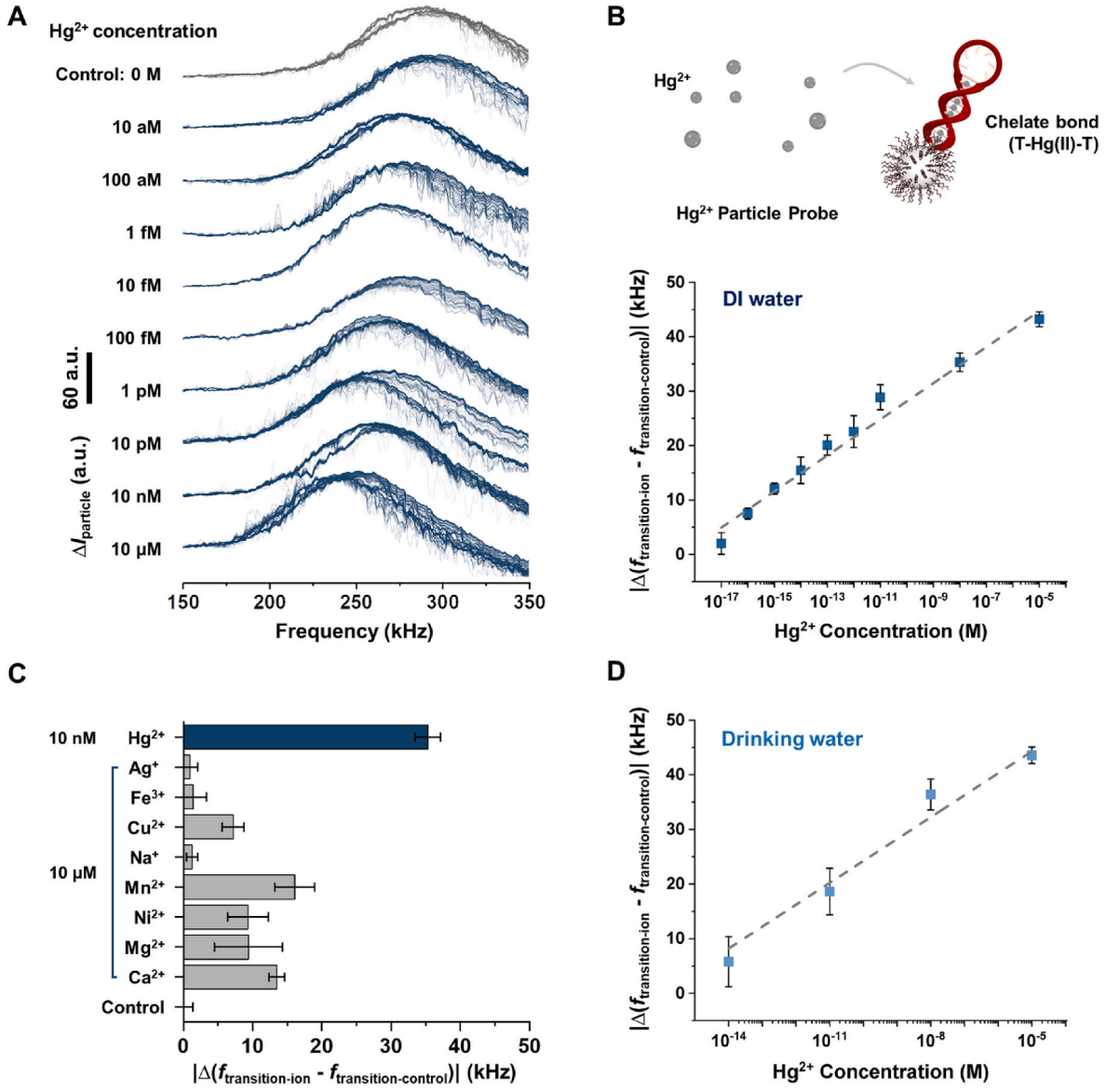

Fig. 4. Characterization of surface charge variation for mercury ions (Hg^{2+}) binding aptamers with respect to Hg^{2+} concentration. (**A**) Measured $\Delta I_{particle}$ data corresponding to the vertical movement of the 28 nt-Hg^{2+} ion functionalized particle probes with different concentrations as a function of DEP frequency. (**B**) $|\Delta(f_{transition-ion} - f_{transition-control})|$ as a function of Hg^{2+} concentration in DI water, indicating significant differences between neighboring concentrations ($p < 0.0001$) (**C**) Selectivity of the developed detection method: $|\Delta(f_{transition-ion} - f_{transition-control})|$ measured after 28 nt-coated particle probes interaction with 10 μM of different interference ions (Ag^{+}, Ca^{2+}, Cu^{2+}, Fe^{3+}, Mg^{2+}, Mn^{2+}, Na^{+}, Ni^{2+}), and 10 nM Hg^{2+} ion, respectively. (**D**) Detection of various concentrations of Hg^{2+} ion (10 fM, 10 pM, 10 nM, 10 μM) in drinking water, where $|\Delta(f_{transition-ion} - f_{transition-control})|$ is the absolute variation of transition frequency between with/without metal ion. The statistical analysis results between neighboring samples in Fig. 4B–D are provided in Supplementary Tables S2–S4.

data also show that the lowest concentration detected by the developed system is in attomolar (aM) range, and the limit of detection (LOD) is estimated to be ~5.6 aM in a DI water, which was calculated based on $3\sigma/S$ (where σ is the standard deviation of the control, and S is the slope of the regression line) (Geng et al., 2018; MacDougall and Crummet, 1980).

3.2.2. Selectivity evaluation of the DEP surface charge detection method

The detecting performance of the developed DEP surface charge detection method is presented in Fig. 4C and D. Fig. 4C shows the selectivity of the developed method when 28 nt aptamer probe particles are interacted with diverse interference ions in a solution. Particle probes coated with 28 nt, which is designed to detect Hg^{2+} ions, were introduced in a DI water solution that contains 10 μM of Ag^{+}, Ca^{2+}, Cu^{2+}, Fe^{3+}, Mg^{2+}, Mn^{2+}, Na^{+}, Ni^{2+} or 10 nM of Hg^{2+} ions (detailed measured results in Fig. S4A). Even at a 1000:1 (10 μM: 10 nM) concentration ratio, the measured $|\Delta(f_{transition-ion} - f_{transition-control})|$ values of interference ions are in the range between 1.2 and 16 kHz, while that of 10 nM Hg^{2+} ions is about 35 kHz, as shown in Fig. 4C. This result indicates that the DNA aptamer-functionalized particle probes are affected more significantly by Hg^{2+} ions than by other interference ions, even when the interference ions are 1000 times more concentrated, indicating excellent selectivity for the target ions when the particle probe is decorated with a DNA aptamer specifically designed for the target ion. The sensitivity of the developed method in drinking water (Nestlé Pure Life), was also examined. Since the drinking water contains many different ions and minerals, these materials can non-specifically bind to the particle probes, resulting in degradation of sensing performance (Holland et al., 2011; Saidur et al., 2017). As shown in Fig. 4D, the lowest detected concentration and LOD were shifted from the attomolar range to the femtomolar range, namely, from 5.6 aM to 7.7 fM, in this realistic system (detailed measured results in Fig. S4B). Despite the increase of the LOD in the drinking water model, the detection performance of the developed method with interfering materials is still superior to the previously reported metal ion detection methods using optical detection (Chun et al., 2018; Ke et al., 2014). The more comparison results between our developed method and other detection methods reported in recent literatures for Hg^{2+} estimation are in Table 2A. Our system exhibits better response than those previously reported concerning both linear detection range and LOD. In general, to increase a system sensitivity, some strategy required such as a complicated preparation process (Chun et al., 2018; Gu et al., 2017; Wang et al., 2018) or post-process after Hg^{2+} incubation (Hong et al., 2017; Wang et al., 2021). However, we demonstrated the capability of simple and sensitive technique for Hg^{2+} detection through two-step preparation process (target molecule incubation and probe purification) after DNA aptamer functionalization. Taken together, our developed method would be able to demonstrate extremely sensitive detection of toxic metal ions (compare to previously reported results) using the surface charge detection method.

3.2.3. Label-free multiplex detection capability of the DEP surface charge detection method

Before discussing a label-free multiplex detection, it should be noted that we measured the sensitivity of silver ion (Ag^{+}) using Ag^{+}-specific aptamer probes by the specific interaction between cytosine nucleic base and silver ion(I) (Ono et al., 2008, Torigoe et al., 2012) because Ag^{+} ions were also used to demonstrate a label-free multiplex detection. The detailed results and observation are in Supplementary Note 3, Fig. S5 and Table S11, indicating wide linear detection range (10 pM–10 μM) and excellent LOD (i.e. 115 fM in DI water and 265 fM in the drinking water) even more sensitive than recent Ag^{+} ion detection studies (Table S5). The label-free multiplex detection is demonstrated for the first time using the developed DEP surface charge detection method, to the best of our knowledge. The schematic and image in Fig. 5A describe how to detect Hg^{2+} and Ag^{+} ions using two different particle probes by simultaneously using a 28 nt-coated particle and a 32 nt-coated particle in the exact same environment. The average $f_{transition}$ for simultaneous Hg^{2+} and Ag^{+} ions detection in DI water and drinking water is presented in Fig. 5B and C with different ion concentrations (detailed $\Delta I_{particle}$ data of two different probes in Fig. S6 and Fig. S7). As shown in Fig. 5B and C, the concentration of the two different ions can be clearly distinguished, indicating that the developed DEP surface charge detection method enables multiplex detection of Hg^{2+} and Ag^{+} ions in a wide range of concentrations (pM – μM). The LOD of the developed method is estimated to be 24.1 fM for Hg^{2+} and 2.57 nM for Ag^{+} in a drinking water, even for the multiplex detection of two different ions. These LOD for multiplex detection is good enough to detect the FDA ion concentration standards for Hg^{2+} and Ag^{+} ions in bottled water, which are 9.97 nM and 927 nM, respectively (Title 21, Code of Federal Regulations (CFR), Part 165). Moreover, our proposed strategy, compared to other heavy-metal ion detection, shows the improved analytical performances in terms of LOD when multiplexing detection (Table 2B), indicating that the developed DEP surface charge detection method is promising for use in practical applications.

Table 2
Comparison of analytical performance between the present approach and previous reports for Hg^{2+} detection (A) and simultaneous detection of both Hg^{2+} and Ag^{+} (B).

(A) Hg^{2+} detection

Detection method	Linear range (Molarity)	LOD (Molarity)	Reference
Optical (counting of binding probes)	1×10^{-10}- 1×10^{-7}	2.7×10^{-11}	(Chun et al., 2018)
Fluorescence	1×10^{-9} - 6×10^{-8}	3.9×10^{-10}	(Gu et al., 2017)
Colorimetry	1×10^{-9}- 1×10^{-8}	5.1×10^{-10}	(Li et al., 2018a)
Electrochemical Impedance Analysis	5×10^{-11}- 10^{-7}, 10^{-7}- 10^{-5}	1.6×10^{-12}	(Hong et al., 2017)
Single-walled carbon nanotube Field Effect Transistor	1×10^{-11}- 5×10^{-8}	1.0×10^{-11}	(Wang et al., 2018)
Electrochemical Differential Pulse Voltammetry	1×10^{-12}- 1×10^{-6}	2.2×10^{-13}	(Wang et al., 2021)
DEP motion	**1×10^{-14} - 1×10^{-5}**	**7.7×10^{-15}**	**Our work**

(B) Simultaneous detection of both Hg^{2+} and Ag^{+}

Detection method	LOD for Hg^{2+} (Molarity)	LOD for Ag^{+} (Molarity)	Reference
Fluorescence	2.7×10^{-7}	4.5×10^{-7}	(Chen et al., 2018)
Colorimetry	5.7×10^{-7}	1.92×10^{-6}	(Phichi et al., 2020)
Fluorescence	1.3×10^{-12}	3.4×10^{-11}	(Ravikumar et al., 2018)
Fluorescence	4.8×10^{-9}	1.0×10^{-9}	(Ren et al., 2017)
Fluorescence	7.9×10^{-7}	2.5×10^{-7}	(Xiao et al., 2021)
DEP motion	**2.4×10^{-14}**	**2.6×10^{-9}**	**Our work**

4. Conclusion

We developed a novel method to detect the surface charge differences between biomolecule-functionalized particle probes through an optical observation of the dielectrophoretic behaviors of numerous particle probes. As a proof of concept for the developed method, the dielectrophoretic (DEP) vertical movements of numerous plain particle probes were monitored by an optical microscope while varying electrical frequency. Using the image sequences that recorded the probes' vertical movements, we mapped the height variation of individual proves to $\Delta I_{particle}$, the brightness variation of each probe on an electrical frequency spectrum. In addition, we defined the transition frequency, $f_{transition}$, based on $\Delta I_{particle}$ on the frequency spectrum in combination with two linear regression-based models. The four important types of

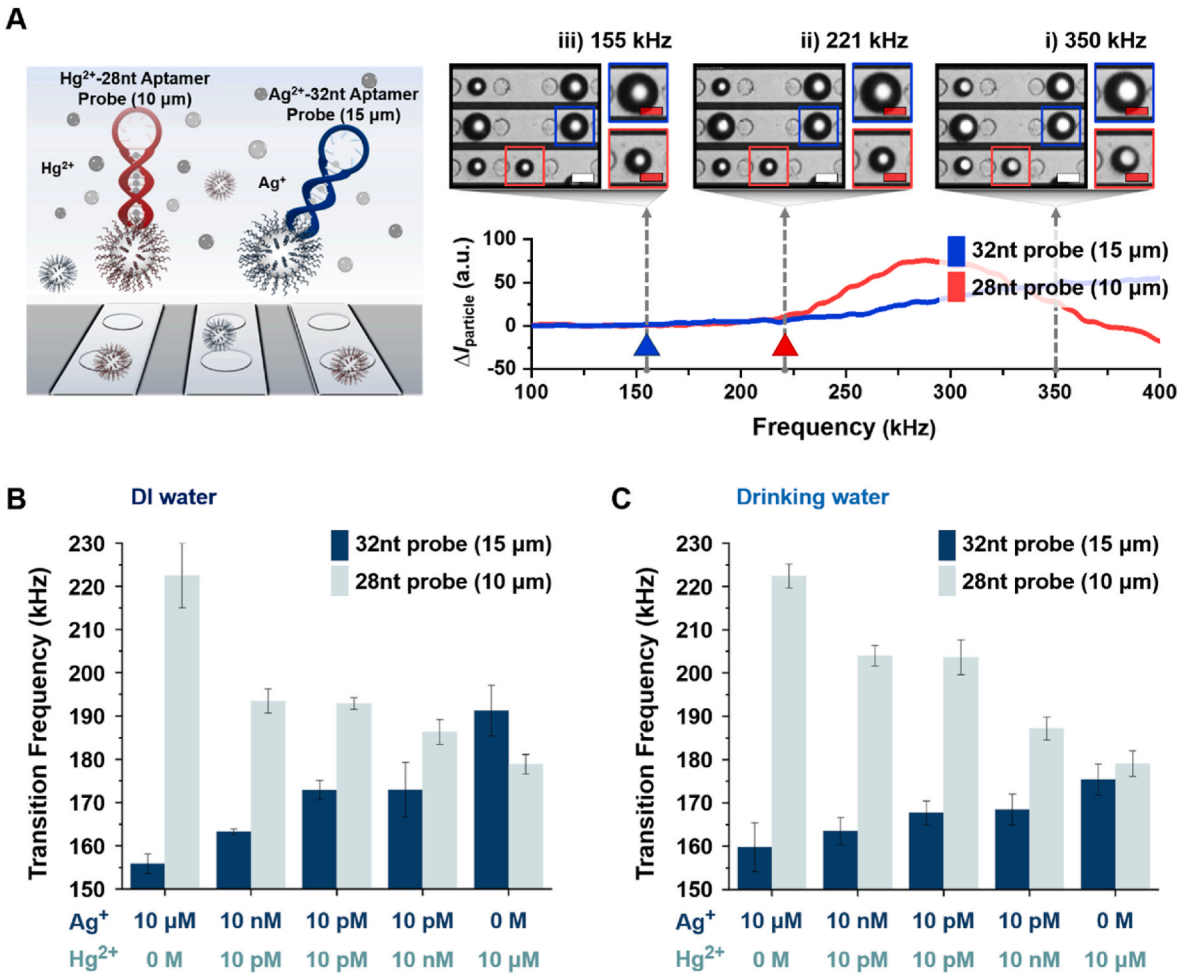

Fig. 5. Multiplex detection of two different target ions. (**A**) Schematic and real measurement images of three different frequencies (350, 221, 155 kHz) with 0.6 $V_{p\text{-}p}$ input voltage that describes multiplex detection using 28 nt aptamer probes (radius: 10 μm) for Hg^{2+} detection and 32 nt aptamer probes (radius: 15 μm) Ag^{+} detection (white scale bar 15 μm and red scale bar 10 μm). The right images and graph of A correspond to 10 μM Ag^{+} vs. 0 M Hg^{2+} concentrations. The $\Delta I_{particle}$ graph of each single particle is shown with its transition frequency. The transition frequency of the 10 μm-28 nt particle is 221 kHz (red triangle) and that of the 15 μm-32nt particle is 155 kHz (blue triangle). (**B**) and (**C**) A comparison of the average measured $f_{transition}$ for Hg^{2+} and Ag^{+} ions at the five different multiplex concentrations of 10 μM Ag^{+} vs. 0 M Hg^{2+}, 10 nM Ag^{+} vs. 10 pM Hg^{2+}, 10 pM Ag^{+} vs. 10 pM Hg^{2+}, 10 pM Ag^{+} vs. 10 nM Hg^{2+}, and 0 M Ag^{+} vs. 10 μM Hg^{2+} in DI water and drinking water, respectively. The statistical analysis results between the data of pure sample and multiplex sample in Fig. 5C and D are provided in Supplementary Tables S6–S7.

biomolecule-functionalized probes were examined by the measurement of the novel parameters, indicating that the developed method can be used for the detection of surface charge differences generated from various biomolecules. The sensitivity and selectivity of using the developed method were also evaluated with the Hg^{2+}-specific binding DNA aptamer. Results indicated that the LOD is around atto- and femtomolar ranges in DI water and in a drinking water, respectively. Furthermore, the developed method showed excellent specificity to the target ion, which demonstrated that the developed detection method is ultra-sensitive and extremely selective. Lastly, two different ions, Hg^{2+} and Ag^{+}, were simultaneously detected using the developed method, showing label-free dielectrophoretic multiplex detection capability. The multiplex detection of two different ions was successful in a wide concentration range (pM – μM) with an LOD of 24.1 fM for Hg^{2+} and 2.57 nM for Ag^{+} in a drinking water, which is sufficient for detecting the FDA standard in bottled water. Altogether, the excellent performance of the label-free DEP multiplex detection using the surface charge differences of biomolecule-functionalized particle probes was demonstrated for the first time. These studies can be useful to implement a platform for the ultra-sensitive multiplex detection of heavy metal ion and open a new avenue for multiplex detection using surface charge/potential differences inside a micro-dielectrophoretic chip.

CRediT authorship contribution statement

Kang In Yeo: Data curation, Formal analysis, Methodology, Writing – original draft. **Insu Park:** Formal analysis, Investigation, Validation, Writing – original draft. **Sang Hyun Lee:** Data curation, Methodology. **Sei Young Lee:** Formal analysis, Writing – review & editing. **Woo-Jin Chang:** Validation, Writing – review & editing. **Rashid Bashir:** Validation, Writing – review & editing. **Seungyeop Choi:** Conceptualization, Investigation, Formal analysis, Methodology, Validation, Writing – original draft. **Sang Woo Lee:** Conceptualization, Investigation, Supervision, Validation, Funding acquisition, Writing – review & editing.

Declaration of competing interest

The authors declare that they have no known competing financial interests or personal relationships that could have appeared to influence the work reported in this paper.

Acknowledgments

This work was supported by National Research Foundation of Korea (NRF) grants funded by the Korean government (NRF-2021R1F1A1046496).

Appendix A. Supplementary data

Supplementary data to this article can be found online at https://doi.org/10.1016/j.bios.2022.114235.

References

Abd Rahman, N., Ibrahim, F., Yafouz, B., 2017. Sensors 17 (3), 449.
Arnold, W.M., Schwan, H.P., Zimmermann, U., 1987. J. Phys. Chem. 91 (19), 5093–5098.
Chalklen, T., Jing, Q., Kar-Narayan, S., 2020. Sensors 20 (19), 5605.
Chen, C., Du, Y., Li, J., Yang, X., Wang, E., 2012. Anal. Chim. Acta 738, 45–50.
Chen, C., Wang, J., 2020. Analyst 145 (5), 1605–1628.
Chen, Q., Yuan, Y.J., 2019. RSC Adv. 9 (9), 4963–4981.
Chen, S., Dong, H., Yang, J., 2020. Sensors 20 (6), 1690.
Chen, S., Wang, W., Yan, M., Tu, Q., Chen, S.-W., Li, T., Yuan, M.-S., Wang, J., 2018. Sensor. Actuator. B Chem. 255, 2086–2094.
Chen, T.-Y., Yang, T.-H., Wu, N.-T., Chen, Y.-T., Huang, J.-J., 2017. Sensor. Actuator. B Chem. 244, 642–648.
Chiu, C.W., Ducker, W.A., 2014. Langmuir 30 (1), 140–148.
Choi, S., Ko, K., Lim, J., Kim, S., Woo, S.-H., Kim, Y., Key, J., Lee, S., Park, I., Lee, S., 2018. Sensors 18 (10), 3543.
Choi, S., Lee, G., Park, I.S., Son, M., Kim, W., Lee, H., Lee, S.-Y., Na, S., Yoon, D.S., Bashir, R., Park, J., Lee, S.W., 2016. Anal. Chem. 88 (22), 10867–10875.
Chun, H.J., Kim, S., Han, Y.D., Kim, D.W., Kim, K.R., Kim, H.-S., Kim, J.-H., Yoon, H.C., 2018. Biosens. Bioelectron. 104, 138–144.
Díaz-González, M., de la Escosura-Muñiz, A., Fernandez-Argüelles, M.T., Alonso, F.J.G., Costa-Fernandez, J.M., 2020. Quantum Dot bioconjugates for diagnostic applications. In: Puente-Santiago, A.R., Rodríguez-Padrón, D. (Eds.), Surface-modified Nanobiomaterials for Electrochemical and Biomedicine Applications. Springer, Cham., Switzerland, pp. 133–176.
Fan, Y., Wang, S., Zhang, F., 2019. Angew. Chem. Int. Ed. 58 (38), 13208–13219.
Geng, F., Jiang, X., Wang, Y., Shao, C., Wang, K., Qu, P., Xu, M., 2018. Sensor. Actuator. B Chem. 260, 793–799.
Goode, J.A., Rushworth, J.V.H., Millner, P.A., 2015. Langmuir 31 (23), 6267–6276.
Grieshaber, D., MacKenzie, R., Vörös, J., Reimhult, E., 2008. Sensors 8 (3), 1400–1458.
Gu, W., Pei, X., Cheng, Y., Zhang, C., Zhang, J., Yan, Y., Ding, C., Xian, Y., 2017. ACS Sens. 2 (4), 576–582.
Hoettges, K.F., Hübner, Y., Broche, L.M., Ogin, S.L., Kass, G.E.N., Hughes, M.P., 2008. Anal. Chem. 80 (6), 2063–2068.
Holland, J.G., Malin, J.N., Jordan, D.S., Geiger, F.M., 2011. J. Am. Chem. Soc. 133 (8), 2567–2570.
Hölzel, R., Pethig, R., 2020. Micromachines 11 (5), 533.
Hong, M., Wang, M., Wang, J., Xu, X., Lin, Z., 2017. Biosens. Bioelectron. 94, 19–23.
Ke, J., Li, X., Zhao, Q., Hou, Y., Chen, J., 2014. Sci. Rep. 4 (1), 5624.
Khan, N.I., Song, E., 2020. Micromachines 11 (2), 220.
Kim, D.-S., Park, J.-E., Shin, J.-K., Kim, P.K., Lim, G., Shoji, S., 2006. Sensor. Actuator. B Chem. 117 (2), 488–494.
Lee, H., Lee, S.W., Lee, G., Lee, W., Nam, K., Lee, J.H., Hwang, K.S., Yang, J., Lee, H., Kim, S., Lee, S.W., Yoon, D.S., 2018. Nanoscale 10 (2), 538–547.
Li, S., Wei, T., Tang, M., Chai, F., Qu, F., Wang, C., 2018a. Sensor. Actuator. B Chem. 255, 1471–1481.
Li, S., Zhang, C., Wang, S., Liu, Q., Feng, H., Ma, X., Guo, J., 2018b. Analyst 143 (18), 4230–4246.
Liao, Z., Zhang, Y., Li, Y., Miao, Y., Gao, S., Lin, F., Deng, Y., Geng, L., 2019. Biosens. Bioelectron. 126, 697–706.
Liu, X., Wang, Y., Song, Y., 2018. Biosens. Bioelectron. 117, 644–650.
Luo, X., Davis, J.J., 2013. Chem. Soc. Rev. 42 (13), 5944–5962.
MacDougall, D., Crummet, W.B., 1980. Anal. Chem. 52 (14), 2242–2249.
Mayne, L., Lin, C.Y., Christie, S.D.R., Siwy, Z.S., Platt, M., 2018. ACS Nano 12 (5), 4844–4852.
Melitz, W., Shen, J., Kummel, A.C., Lee, S., 2011. Surf. Sci. Rep. 66 (1), 1–27.
Nakano, M., Ding, Z., Matsuda, K., Xu, J., Inaba, M., Suehiro, J., 2019. Biomicrofluidics 13 (6), 064109.
Ono, A., Cao, S., Togashi, H., Tashiro, M., Fujimoto, T., Machinami, T., Oda, S., Miyake, Y., Okamoto, I., Tanaka, Y., 2008. Chem. Comm. (39), 4825–4827.
Ono, A., Togashi, H., 2004. Angew. Chem. Int. Ed. 43 (33), 4300–4302.
Pakchin, P.S., Nakhjavani, S.A., Saber, R., Ghanbari, H., Omidi, Y., 2017. TrAC Trends Anal. Chem. (Reference Ed.) 92, 32–41.
Park, C., Jang, K., Lee, S., You, J., Lee, S., Ha, H., Yun, K., Kim, J., Lee, H., Park, J., Na, S., 2015a. Nanotechnology 26 (30), 305501.
Park, I., Lim, J.W., Kim, S.H., Choi, S., Ko, K.H., Son, M.G., Chang, W.-J., Yoon, Y.R., Yang, S., Key, J., Kim, Y.S., Eom, K., Bashir, R., Lee, S.Y., Lee, S.W., 2020. J. Phys. Chem. Lett. 11 (17), 7197–7203.
Park, I.S., Eom, K., Son, J., Chang, W.J., Park, K., Kwon, T., Yoon, D.S., Bashir, R., Lee, S. W., 2012. ACS Nano 6 (10), 8665–8673.
Park, I.S., Kwak, T.J., Lee, G., Son, M., Choi, J.W., Choi, S., Nam, K., Lee, S.-Y., Chang, W.-J., Eom, K., Yoon, D.S., Lee, S., Bashir, R., Lee, S.W., 2016. ACS Nano 10 (4), 4011–4019.
Park, I.S., Lee, J., Lee, G., Nam, K., Lee, T., Chang, W.-J., Kim, H., Lee, S.-Y., Seo, J., Yoon, D.S., Lee, S.W., 2015b. Anal. Chem. 87 (12), 5914–5920.
Park, I.S., Park, S.H., Yoon, D.S., Lee, S.W., Kim, B.-M., 2014a. Appl. Phys. Lett. 105 (10), 103701.
Park, J., Lee, S., Jang, K., Na, S., 2014b. Biosens. Bioelectron. 60, 299–304.
Phichi, M., Imyim, A., Tuntulani, T., Aeungmaitrepirom, W., 2020. Anal. Chim. Acta 1104, 147–155.
Pourali, A., Rashidi, M.R., Barar, J., Pavon-Djavid, G., Omidi, Y., 2021. TrAC Trends Anal. Chem. (Reference Ed.) 134, 116123.
Ravikumar, A., Panneerselvam, P., Morad, N., 2018. ACS Appl. Mater. Interfaces 10 (24), 20550–20558.
Ren, G., Zhang, Q., Li, S., Fu, S., Chai, F., Wang, C., Qu, F., 2017. Sensor. Actuator. B Chem. 243, 244–253.
Ronkainen, N.J., Halsall, H.B., Heineman, W.R., 2010. Chem. Soc. Rev. 39 (5), 1747–1763.
Saidur, M.R., Aziz, A.R.A., Basirun, W.J., 2017. Biosens. Bioelectron. 90, 125–139.
Shahim, S., Sukesan, R., Sarangadharan, I., Wang, Y.L., 2019. Sensors 19 (9), 1969.
Shan, B., Pu, Y., Chen, Y., Liao, M., Li, M., 2018. Coord. Chem. Rev. 371, 11–37.
Shi, W., Friedman, A.K., Baker, L.A., 2017. Anal. Chem. 89 (1), 157–188.
Sinensky, A.K., Belcher, A.M., 2007. Nat. Nanotechnol. 2 (10), 653–659.
Son, M., Choi, S., Ko, K.H., Kim, M.H., Lee, S.-Y., Key, J., Yoon, Y.-R., Park, I.S., Lee, S. W., 2016. Langmuir 32 (3), 922–927.
Su, L., Jia, W., Hou, C., Lei, Y., 2011. Biosens. Bioelectron. 26 (5), 1788–1799.
Torigoe, H., Miyakawa, Y., Ono, A., Kozasa, T., 2012. Thermochim. Acta 532, 28–35.
Vacic, A., Criscione, J.M., Stern, E., Rajan, N.K., Fahmy, T., Reed, M.A., 2011. Biosens. Bioelectron. 28 (1), 239–242.
Viefhues, M., Eichhorn, R., 2017. Electrophoresis 38 (11), 1483–1506.
Vorwerg, L., Antonietti, M., Tauer, K., 1999. Colloids Surf. A Physicochem. Eng. Asp. 150 (1), 129–135.
Vu, C.-A., Chen, W.-Y., 2019. Sensors 19 (19), 4214.
Wang, H., Liu, Y., Liu, G., 2018. ACS Sens. 3 (3), 624–631.
Wang, X., Xu, C., Wang, Y., Li, W., Chen, Z., 2021. Sensor. Actuator. B Chem. 343, 130151.
Xiao, L., Liu, K., Duan, L., Cheng, X., 2021. J. Mater. Chem. C 9 (14), 4877–4887.
Yafouz, B., Kadri, N.A., Ibrahim, F., 2014. Sensors 14 (4), 6356–6369.
Yáñez-Sedeño, P., Campuzano, S., Pingarrón, J.M., 2017. Sensors 17 (5), 965.
Yin, H., Truskewycz, A., Cole, I.S., 2020. Microchim. Acta 187 (6), 336.